

A multi-wavelength scattered light analysis of the dust grain population in the GG Tau circumbinary ring

G. Duchêne, C. McCabe, A. M. Ghez

Division of Astronomy and Astrophysics, UCLA, Los Angeles, CA 90095-1562

duchene@astro.ucla.edu

B. A. Macintosh

Lawrence Livermore National Laboratory, 7000 East Avenue, Livermore, CA 94550-9234

ABSTRACT

We present the first $3.8\ \mu\text{m}$ image of the dusty ring surrounding the young binary system GG Tau, obtained with the W. M. Keck II 10 m telescope's adaptive optics system. This is the longest wavelength at which the ring has been detected in scattered light so far, allowing a multi-wavelength analysis of the scattering properties of the dust grains present in this protoplanetary disk in combination with previous, shorter wavelengths, *HST* images. We find that the scattering phase function of the dust grains in the disk is only weakly dependent on the wavelength. This is inconsistent with dust models inferred from observations of the interstellar medium or dense molecular clouds. In particular, the strongly forward-throwing scattering phase function observed at $3.8\ \mu\text{m}$ implies a significant increase in the population of large ($\gtrsim 1\ \mu\text{m}$) grains, which provides direct evidence for grain growth in the ring. However, the grain size distribution required to match the $3.8\ \mu\text{m}$ image of the ring is incompatible with its published $1\ \mu\text{m}$ polarization map, implying that the dust population is not uniform throughout the ring. We also show that our $3.8\ \mu\text{m}$ scattered light image probes a deeper layer of the ring than previous shorter wavelength images, as demonstrated by a shift in the location of the inner edge of the disk's scattered light distribution between 1 and $3.8\ \mu\text{m}$. We therefore propose a stratified structure for the ring in which the surface layers, located $\sim 50\ \text{AU}$ above the ring midplane, contain dust grains that are very similar to those found in dense molecular clouds, while the region of the ring located $\sim 25\ \text{AU}$ from the midplane contains significantly larger grains. This stratified structure is likely the result of vertical dust settling and/or preferred grain growth in the densest parts of the ring.

Subject headings: planetary systems: protoplanetary disks — dust, extinction — scattering — stars: individual (GG Tau)

1. Introduction

The process of planet formation is thought to occur during the first few million years of the evolution of a star, i.e. during its pre-main-sequence phase for low-mass objects. The generally accepted scenario of planet formation, as articulated originally by Safranov (1969), starts with an initial population of small, interstellar medium (ISM)-like particles growing by coagulation to form km-sized bodies, whose gravitational well is then deep enough to ignite a runaway accretion process of all dust and gas located at similar distances from the central object. Numerical models of dust coagulation suggest that submicron grains grow to particles several times $10\ \mu\text{m}$ or more in radius in less than 10^4 yrs in the densest parts of protoplanetary disks (e.g. Weidenschilling 1980; Suttner & Yorke 2001). Coagulation of small planetesimals into larger bodies may then occur on timescales as short as 10^5 yrs (e.g., Wetherill & Stewart 1993), with planetary cores ($R > 10^3$ km) eventually forming within a few AU of the central star over a timescale of $\lesssim 10$ Myr (e.g., Pollack et al. 1996; Kenyon & Bromley 2003). Observationally, however, the timescales associated with each of these stages of the planet formation process are poorly constrained. Using the fraction of stars with a near-infrared excess within star-forming regions of different ages as a proxy for disk evolution, Haisch, Lada & Lada (2001) estimate that the inner disk region is completely cleared of μm -sized particles in $\lesssim 10$ Myr. Whether this timescale corresponds to the end of the runaway accretion phase of planetesimals or to the disk dispersal through accretion onto the star is unknown. In any event, to study grain growth during the planet formation process, it is necessary to establish the properties of dust grains in disks surrounding Myr-old T Tauri stars.

The search for empirical evidence of grain growth in protoplanetary disks began through investigations that probed the (sub)millimeter thermal emission properties of the dust. In this regime, the disks are largely optically thin, which allows for relatively simple modeling. The large dust opacities (Beckwith et al. 1990) and shallow spectral index of the disk thermal emission (e.g., Beckwith & Sargent 1991; Mannings & Emerson 1994) disagree with the expected behavior of ISM-like dust grains and suggest that mm-sized grains are present in most T Tauri circumstellar disks. Analyses of the entire disk spectral energy distribution has recently led to similar conclusions (D’Alessio, Calvet & Hartmann 2001; Wood et al. 2002). However, in order to devise an accurate model of the thermal emission from a circumstellar disk, the outer radius and vertical structure must be determined from spatially resolved images; in the many cases where this is not possible, degeneracies between the dust temperature, total mass and opacity are left unsolved and cause large uncertainties in the size distribution (e.g., Chiang et al. 2001).

A second approach used to determining the properties of dust grains in circumstellar

disks is through high angular resolution scattered light images in the visible or near-infrared. At these wavelengths, a typical T Tauri disk is optically thick; the photons, which are scattered off the surface layer of the disk, therefore provide information on the global geometric properties of the disk, such as its radius, total height and amount of flaring. More importantly, the scattering process is dependent on the size distribution of dust grains present in the disk. In the Mie theory, which assumes scattering off spherical particles, the scattering is a strong function of the dust grain “size parameter” ($x = 2\pi a/\lambda$, where a is the grain radius), with scattered light images being most sensitive to grains in the range $0.5 \lesssim x \lesssim 3$. Multi-wavelength scattered light studies of disks therefore provide direct information on the dust grain size distribution. For instance, scattered light observations in the visible and near-infrared ($1\text{--}2\ \mu\text{m}$) are sensitive to grains that are, at most, $1\ \mu\text{m}$ in size. Such observations alone are therefore not enough to reach firm conclusions regarding grain growth with respect to ISM particles, as the largest grains ISM grains have inferred radii $\lesssim 1\ \mu\text{m}$ (e.g., Mathis & Whiffen 1989; Kim, Martin & Hendry 1994; Weingartner & Draine 2001).

Extending this multi-wavelength scattered light approach to even longer wavelengths, i.e., in the thermal infrared regime ($> 3\ \mu\text{m}$), can allow one to probe the presence of grains several microns in size, which are explicitly larger than those found in the ISM and at least as large as those found in dense molecular clouds (Weingartner & Draine 2001). A powerful approach to determining the dust grain size distribution, therefore consists in obtaining several images of the same protoplanetary disk over a wide range of wavelengths, ideally from the visible to the mid-infrared. If this can be achieved, the wavelength-dependence of the scattered light informs us directly on the size distribution of dust grains as the disk geometry is fixed and the detailed composition of the grains only plays a limited role in their scattering properties. In a recent study, we have obtained the first $11.8\ \mu\text{m}$ scattered light image of the edge-on disk system HK Tau B, which has clearly revealed the presence of dust grains up to $\sim 3\ \mu\text{m}$ (McCabe, Duchêne & Ghez 2003).

We present here the first spatially-resolved $3.8\ \mu\text{m}$ image of the dusty torus surrounding the young (1 Myr) GG Tau A binary system¹. This disk, first discovered through its thermal emission by millimeter interferometry (Simon & Guilloteau 1992; Guilloteau, Dutrey & Simon 1999), is a massive ($0.13 M_{\odot}$) torus with inner and outer radii of 180 and 260 AU located at a distance of 140 pc (Bertout, Robichon & Arenou 1999). The inner binary, which has a projected separation of 35 AU (Leinert et al. 1991; Ghez, Neugebauer & Matthews 1993), has carved out a central gap through its orbital motion, explaining the large inner radius of the ring. Since its discovery, the ring has been spatially resolved in scattered light at various

¹GG Tau is a hierarchical quadruple system, with a $10''$ separation between GG Tau A and GG Tau B. In the following, we only consider GG Tau A, which we refer to as GG Tau for simplicity.

wavelengths ranging from 0.6 to $2\ \mu\text{m}$ (Roddier et al. 1996; Silber et al. 2000; McCabe, Duchêne & Ghez 2002; Krist, Stapelfeldt & Watson 2002; Itoh et al. 2002). Models of the scattered light images of the ring have both concluded for and against grain growth in the disk (Wood, Crosas & Ghez 1999; Krist et al. 2002; McCabe et al. 2002), mostly because of their limited wavelength coverage.

Our new $3.8\ \mu\text{m}$ image of the GG Tau torus clearly shows that the deeper parts of the disk contain larger grains than the surface layers, and that they are even larger than those found in the ISM or in molecular clouds. The outline of this paper is as follows: the observations and data reduction processes are summarized in §2, while the results are presented in §3. Multi-wavelength Monte Carlo models of the ring are presented in §4. The properties of dust grains in the ring are discussed in §5 and §6 summarizes our conclusions.

2. Observations and data analysis

The data presented here were obtained with the W. M. Keck II 10 m telescope on 2002 December 12 & 13, using the facility NIRC2 instrument (K. Matthews et al., in prep.) installed behind the adaptive optics (AO) system (Wizinowich et al. 2000). With a 1024^2 detector and employing a pixel scale of $0.00994''/\text{pix}$, the instrument offers a field of view of $\sim 10''$. We used the L' filter ($\lambda_0 = 3.78\ \mu\text{m}$, $\Delta\lambda = 0.70\ \mu\text{m}$) throughout the observations. A circular cold pupil mask, equivalent to a 9 m entrance pupil (largest circle inscribed in the hexagonal primary mirror), was used to reduce the thermal background and smooth out the complex, hexagonal shape of the telescope’s point spread function (PSF). GG Tau itself ($R = 11.2\ \text{mag}$, Kenyon & Hartmann 1995) was used as guide star for the AO system, which was running at a frequency of about 100 Hz. The resulting AO correction was stable throughout the run, with typical Strehl ratios on order of 60% as measured on images of single stars relative to the 9 m pupil employed for our observations. From a gaussian fit to images of single stars, we estimate that the spatial resolution of our dataset is about $0''.091$ (FWHM).

The photometric standard HD 1160 ($L' = 7.04\ \text{mag}$, Bouchet, Schmider & Manfroid 1991; Tinney, Mould & Reid 1993) was observed on both nights of the observing run. Aperture photometry was performed on this object with a circular aperture of $1''.44$ and measuring the sky level in an annulus from $1''.49$ to $1''.79$. This allowed us to estimate our absolute calibration scale to within $\sigma_{L'} = 0.13\ \text{mag}$. The airmass extinction was derived through the repeated observations of CI Tau during the run (see below) and we found an extinction coefficient of $0.048\ \text{mag/airmass}$ on both nights.

Short exposures (0.181 s) of the GG Tau system were obtained in order to avoid saturation of the strong thermal background at these wavelengths; 300 such exposures obtained at a given position on the chip were coadded into a single image before nodding to another position. We used a 4-position pattern defined so that the whole ring would fit in the detector on each individual image without overlap between consecutive images. Over the two nights, we integrated for 32 such cycles on target, i.e. 128 independent images amounting to 6950 s of integration (1h56min). The images of GG Tau were interleaved with observations of blank sky fields and of isolated nearby stars to estimate the instrumental PSF with a setup that reproduced the same conditions for the AO system. We mostly used CI Tau ($R = 12.2$ mag, Kenyon & Hartmann 1995), another T Tauri star located $\sim 5^\circ$ away from GG Tau, and GJ 9140 ($R = 11.3$ mag, Weis 1996), both of which produced very similar PSFs to the observations of GG Tau. We held the telescope’s pupil orientation fixed throughout the observations, so that the substructures in the wings of the AO-corrected PSF remained stationary which allows for a subsequent better subtraction. Consequently, the actual orientation of the images on the sky continuously rotated at a rate that never exceeded 2° per image and was usually much slower, so that field rotation did not blur our image.

A nightly flat field image was created by medianing and normalizing all images of the sky and of isolated standard stars; 103 and 60 images were used in each night respectively. In the images of single stars, all pixels with fluxes higher than the 3σ noise level were excluded to avoid contamination of the stellar flux in the flat-field. Each image of GG Tau was first sky-subtracted using the image of the same cycle that i) had the object in the opposite corner of the detector and ii) was closest in time, and was then flat-fielded. Because the sky thermal emission is rapidly variable, the sky subtraction did not always yield a zero background. A secondary sky correction was therefore performed by subtracting the median of the two star- and disk-free quadrants from the whole image; this second subtraction typically amounted to $\lesssim 5\%$ of the primary sky subtraction. Finally, the images were bad pixel corrected.

To characterize the disk emission around GG Tau, the much stronger flux from the two components of the binary system had to be removed. This was done through PSF fitting and subtraction. We created a library of 5 PSF images of CI Tau and/or GJ 9140 for each night. Each image is the sky-subtracted shift-and-add average of 1 to 3 consecutive 4-position cycles on the same star. Since we combined only almost contemporaneous images in each PSF image, each night’s PSF library contains a range of AO corrections, which allows for a better fit of each image of GG Tau. We created a PSF fitting routine that extracts information for both components (location and flux) simultaneously, using the built-in IDL global minimization routine `amoeba`, a downhill simplex algorithm (Press et al. 1992), to minimize the residuals within a $0''.5$ radius around each component. Each of the 128 images of GG Tau was PSF fitted using each PSF in the library of the corresponding night; the final

subtracted image used is that which yielded the smallest residuals.

All images were then rotated to a common orientation and shift-and-added using the stars' location measured from the PSF fitting. This was done separately on the datasets with and without PSF subtraction; these final images are presented in Figure 1. Since the NIRC2 pixel scale is 4.5 times smaller than the Nyquist sampling of the spatial resolution of our images, we also applied a smoothing process by replacing each pixel with the median value of a 3 pixel-radius aperture centered on it. This local averaging is performed within less than one resolution element around each pixel, so it does not affect our spatial resolution but it significantly enhances the contrast of the images by decreasing the pixel-to-pixel noise by a factor of ~ 2.5 .

The photometry and astrometry of the GG Tau binary was extracted from the PSF fitting results, using the average and standard deviations of all measurements to estimate the final values and their associated uncertainties. The flux for each individual component is measured on the best-fitting model PSF using aperture photometry within a $0''.50$ -radius aperture, and measuring the sky in an annulus $2''.5$ – $2''.6$ in radius in the actual image of the binary. The fluxes were aperture-corrected: from encircled energy measurements of the best-fitting PSF we find that a $0''.5$ aperture contains 83% of the total flux of any star. The results are summarized in Table 1. The measured flux ratio of the binary ($\Delta L' = 0.59 \pm 0.03$ mag) is significantly different from the L' band ($\lambda_0 = 3.5 \mu\text{m}$, $\Delta\lambda = 0.6 \mu\text{m}$) flux ratio reported by White & Ghez (2001), $\Delta L = 0.87 \pm 0.01$ mag. This probably results from the variability of at least one of the components of the system, although the difference in filter bandpass could account for part of this discrepancy. Regarding the measured astrometric properties of the binary, we have taken into account assumed uncertainties of 0.5% on the instrument plate scale measurement and $0^\circ.5$ on its absolute orientation.

In the following, we adopt the stellar masses derived by White et al. (1999), $M_A = 0.76 M_\odot$ and $M_B = 0.68 M_\odot$, to determine the location of the center of mass of the binary system. More recently, Hartigan & Kenyon (2003) derived $M_A = 0.60 M_\odot$ and $M_B = 0.38 M_\odot$, respectively, using a more elaborate analysis that takes into account the accretion-induced veiling in the stellar spectra. However, their analysis of low- and medium- resolution spectra results in discrepant estimates for the veiling, raising questions about which set of stellar parameters to use. The difference between the two predicted binary mass ratios, $q = 0.89$ from White et al. (1999) and $q = 0.63$ from Hartigan & Kenyon (2003), results in an apparent shift of the center of mass of the binary of about $0''.02$ only, which is a negligible effect for our analysis of the ring properties.

3. Results

3.1. L' properties of the circumbinary disk

Our PSF-subtracted L' image of the GG Tau system reveals a continuous ring around the two stars with its brightest part located at a position angle of $\sim 25^\circ$. The ring is detected at most azimuths above the 2σ detection limit per resolution element, except for the sector at position angles $140\text{--}180^\circ$, and up to $\sim 10\sigma$ at peak brightness.

To quantify the morphology and photometric properties of the ring, we first fitted its structure with an ellipse. We used the same approach as in McCabe et al. (2002), which we briefly describe here. For each 10° sector in position angle, we computed the radial profile of the ring, taking the center of mass of the binary as reference. We then fitted a 4th-order polynomial function to a $\sim 0''.5$ portion of this profile and extracted from this the location of the peak (defined as the midpoint between the inner and outer half-peak radii) and its intensity. The polynomial fit failed for the sectors at position angles $\sim 100^\circ$ and $140\text{--}200^\circ$ due to the faintness of the ring in those areas. Uncertainties in the peak position for each azimuthal profile are defined as the standard deviation of the peak positions measured in four sub-maps of the data. We then fitted an ellipse to the location of the peaks at all available position angles with a χ^2 minimization routine. The best fitting model has a semi-major axis of $1''.48 \pm 0''.02$, an eccentricity of 0.65 ± 0.01 and a position angle of the minor axis of $13^\circ \pm 5^\circ$. The geometrical center of the best fitting ellipse is located $0''.16 \pm 0''.04$ due South from the center of mass of the binary.

Since the apparent morphology of the ring is in agreement with that derived from other images of the ring (see § 3.2), we estimated the photometry of the ring through the same aperture as in McCabe et al. (2002), defined by two concentric, $e = 0.65$ ellipses of radii $0''.99$ and $2''.2$ respectively. The integrated flux of the disk corresponds to 0.97% of the integrated starlight from both components (with a relative uncertainty on the order of 10%), and its peak surface brightness is about $11.3 \text{ mag/arcsec}^2$. Using the same elliptical aperture, we find that the flux ratio between the northern (position angles $275\text{--}95^\circ$) and southern (position angles $95\text{--}275^\circ$) halves of the disk is ~ 2.5 . From the polynomial fits presented above, we constructed an azimuthal intensity profile of the ring (Figure 2), from which we find that the peak-to-peak intensity is ~ 5 , although there are a few sectors of the ring whose (undetected) maximum intensity is $\gtrsim 6$ times fainter than its peak surface brightness. Since the southern half of the ring is much fainter than the northern half, those flux ratios are subject to $20\text{--}30\%$ uncertainties which are dominated by uncertainties in the background subtraction. These results are summarized in Table 2.

3.2. Wavelength dependence of the ring properties

In this section, we compare the properties of the ring observed in our L' image to those obtained at shorter wavelengths by Krist et al. (2002) and McCabe et al. (2002). In spite of a significantly higher background noise due to the atmosphere’s thermal emission at $3.8\ \mu\text{m}$, our new image is of high enough quality to allow us to measure significant wavelength-dependent effects. Given the very low temperature of the dust in the ring ($35\ \text{K}$, Guilloteau et al. 1999), we can only be detecting scattered starlight off the ring at $3.8\ \mu\text{m}$. This is so far the longest wavelength at which this structure has been detected in scattered light. Quantifying the chromatic effects in the ring images will help us constrain the properties of the dust population.

Table 2 summarizes several quantities extracted from our L' image, as well as from the J and H band images presented in McCabe et al. (2002). Their K band image is not used in this analysis as it was inadvertently taken out of focus, preventing an accurate estimate of the azimuthal surface brightness distribution of the ring at that wavelength. The quantities we consider here are the integrated disk/star (R_λ) and front/back (FB_λ) flux ratios of the ring, as well as the distance between the center of mass of the system and the peak of the scattered light flux (D_{peak}) in the ring’s radial profiles around position angle 7° , i.e., along its semi-minor axis. We have also measured these same quantities from the $HST/WFPC2$ images obtained by Krist et al. (2002) with the F814W filter, a close match to the usual I filter. Since this image has a very similar signal-to-noise as the J band image from McCabe et al. (2003), we assigned the same uncertainties to both wavelengths. We now have an homogeneous set of quantities that characterize the disk surface brightness and that can be compared to each other.

We first consider the apparent geometry of the ring. The ellipse that best fits the L' image of the ring is in excellent agreement with that fit by McCabe et al. (2002) to the near-infrared images of the ring. Assuming that it has an intrinsically circular shape, the observed aspect ratio of the ring at L' implies an inclination of about $40^\circ \pm 1^\circ$, somewhat larger than that derived from the millimeter thermal emission ($37^\circ \pm 1^\circ$, Guilloteau et al. 1999). As discussed in McCabe et al. (2002), this difference is the result of the geometrical *and* optical thickness of the ring. This implies that the ring is still optically thick to the illuminating starlight at $3.8\ \mu\text{m}$.

Although the global shape of the ring is consistent with previous images, a subtle though significant wavelength-dependent effect can be noted in our image: the distance between the center of mass of the system and the northern edge of the disk along the semi-minor axis of the system increases toward longer wavelength. This distance was measured to be $0''.88$ in the near-infrared by McCabe et al. (2002). In the I band image of Krist et al. (2002), we

measure this distance to be $0''.87$, consistent with the value measured in the near-infrared. On the other hand, the equivalent distance in our L' image² is $0''.97$. This shift, significant at the 5σ confidence level (cf Table 2), is clearly illustrated in Figure 3. If the ring was geometrically thin, scattered light would be detected at a distance $R_{in} \cos i$ from the center of mass which can be inferred from the dust millimeter thermal emission; both distances measured in the scattered light images are significantly smaller than this value. This offset has already been noted in the past and convincingly interpreted as evidence that the ring is optically thick up to high elevations above its midplane (Guilloteau et al. 1999; McCabe et al. 2002). The amplitude of the offset is proportional to the actual height up to which the ring is optically thick. Our new result, namely that this offset decreases toward longer wavelengths, indicates that the dust opacity in the ring decreases enough to bring the dominant scattering layer significantly closer to the ring midplane. With $R_{in} = 190$ AU (see § 5.1) and $i = 37^\circ$ (Guilloteau et al. 1999), we find that scattering of the $\lambda \lesssim 2 \mu\text{m}$ starlight toward the observer predominantly occurs about 50 AU above the ring midplane, while it is only 25 AU for the L' photons. Note that the offsets measured in the I , J and H images are consistent with each other at the $\lesssim 2\sigma$ confidence level, indicating that all three wavelengths roughly probe the same layer of the ring.

Besides the geometrical appearance of the ring, we also searched for photometric changes with wavelength. The total disk/star flux ratio displays significant variations from the visible to the thermal infrared. The ring color excess indices (with respect to the stars) are $\Delta(I - J) = 0.08 \pm 0.05$ mag, $\Delta(J - H) = 0.10 \pm 0.03$ mag and $\Delta(J - L) = -0.40 \pm 0.10$ mag. Overall, we find that the ring tends to become comparatively redder than the central stars toward shorter wavelength, a trend that continues into the visible ($\Delta(V - I) \sim 0.8$ mag, Krist et al. 2002). The distribution of scattered light around the stars, on the other hand, is almost independent of wavelength. The position angle of the ring's brightest point at L' is fully consistent with that of shorter wavelength images. Similarly, the undetected portion of the ring in our image has consistently been found as the faintest in previous high contrast images of the GG Tau system. More generally, the azimuthal intensity profile of the ring at L' is remarkably similar to those observed at shorter wavelengths, as illustrated in Figure 2. The largest chromatic effect we identify is the slight increase of the peak-to-peak front/back flux ratio, which is typically 3–4 at I , J and H (averaged over 5° - to 10° -sectors). Still, this effect is marginal.

²The NIRC2 detector has a well-characterized distortion pattern that introduces a $\lesssim 1$ pixel, or $0''.01$, error in a $\sim 1''$ -distance measurement in any image of the ring, which is negligible compared to the $0''.09$ shift measured here. Furthermore, since our final image is an average of many images taken at 4 different locations on the detector and over a $\sim 180^\circ$ -range of orientations, we assume that the distortion effect is actually even smaller.

Overall, the GG Tau ring scattered light images appear to be only weakly dependent on wavelength, except for the distance between the center of mass of the system and the closest edge of the ring, which is larger at $3.8\ \mu\text{m}$ than at all other wavelengths. As our Monte Carlo modeling shows (§ 4), this absence of strong chromatic variations in the ring proves that grains larger than $1\ \mu\text{m}$ are present, therefore that grain growth has occurred in this environment (§ 5).

4. Scattering models

Our goal is to devise a comprehensive model that reproduces all scattered light images of the GG Tau ring, namely the *I* band *HST*/WFPC2 image from Krist et al. (2002), the *J* and *H* *HST*/NICMOS we have already obtained (McCabe et al. 2002) and the new *L'* image presented here. Attempting to reproduce simultaneously visible, near- and thermal infrared images of the ring will provide stringent constraints on the dust grain properties, and particularly their size distribution.

For this analysis, we have conducted a number of numerical simulations that calculate the multiple scattering of photons emitted from the central stars off the ring. We used the same Monte Carlo code as in McCabe et al. (2002), and only present here its most important input parameters and assumptions (§ 4.1). We then summarize the generic trends revealed by these models as a function of wavelength and dust grain size and identify a range of models that reasonably reproduce each available image of the GG Tau disk (§ 4.2).

4.1. Framework of the Monte Carlo simulations

Our numerical model (Ménard 1989; Duchêne 2000) randomly propagates light packets (“photons”) in all directions from the central object, which we treat for simplicity as a single star having the integrated stellar light properties³. The circumstellar material density is tabulated in a cylindrical coordinate system and we assume that the system is azimuthally symmetric. Photons that reach the ring are scattered after a random optical depth taken from an $e^{-\tau}$ probability distribution. The size of the dust grain that the photon scatters

³Krist et al. (2002) concluded that including explicitly two stars in the simulations has only a very marginal effect on the resulting synthetic images of the GG Tau ring.

off is randomly selected in the scattering cross section-weighted size distribution⁴, and the associated Stokes transfer matrix is calculated through Mie theory. The grains are assumed to be spherical or, if elongated, randomly oriented so that their average cross-section is isotropic. At each scattering event, photons lose a fraction (on the order of the dust albedo) of their incoming intensity and photons that have experienced more than 30 scatterings are terminated as they carry a negligible intensity. We ran 4 million photons per simulation and created synthetic intensity maps by collecting all photons that leave the ring with an inclination from the line of sight in the range 32–37°, similar to the system’s inclination (37°). Considering the 37–41° inclination range instead leads to similar conclusions; this choice is therefore not critical for our analysis. The size of the output images is about 4''3 on a side, sampled at 0''.042/pixel.

To focus our analysis on the dust grain properties, we adopted the same ring geometry for all models. We initially assumed the ring geometry estimated from the (optically thin) millimeter thermal emission by Guilloteau et al. (1999). The relevant model parameters here are: the inner and outer radii (180 AU and 260 AU), the total dust mass ($0.0013 M_{\odot}$), the vertical scale height (32 AU at the inner edge), the flaring index ($H(r) \propto r^{1.05}$) and the surface density distribution ($\Sigma(r) \propto r^{-1.7}$). Under the assumptions of vertical hydrostatic equilibrium and isothermality, we tabulated the density distribution of dust surrounding the binary in a 300 AU-radius cylinder. We neglect the presence of the outer disk seen in CO emission by Guilloteau et al. (1999) as the ring itself is optically thick at all wavelengths considered here, so that virtually no photons scatter off the outer disk. We let the density distribution extend inside of the ring inner radius with a gaussian function attenuation factor described by a $1/e$ width of 7 AU. The amount of material located inside of 180 AU therefore represents a small fraction ($\sim 5\%$) of the total disk mass. Because this geometry does not provide a perfect match to the images of the disk (see § 5.1), we increased the inner radius to 190 AU and reduced the $1/e$ width of the inner radius cutoff to 2 AU. These are the values used in all the models discussed quantitatively in the following.

We assumed the composite, porous dust grain properties from Mathis & Whiffen (1989, their model A), resulting in a 0.5 g/cm^3 average grain density. The numerical models are monochromatic with the central wavelength of the filters (0.8, 1.0, 1.6 and $3.8 \mu\text{m}$ respectively for the *I*, *J*, *H* and *L'* filter) used to match the various observations of the ring. Chromatic changes in the scattering properties within a given bandpass is a second order effect that

⁴While more than 95% of dust grains have radii $a \leq 0.1 \mu\text{m}$ in all of our models, their scattering cross section is so small that they do not account for any significant scattered flux: between 95% and 99% of all scattering events occur on grains larger than $0.1 \mu\text{m}$. It is therefore not advisable to use a simple “effective” grain size, as absorption and scattering are dominated by different dust grains.

we neglect here. The dust grain size distribution is assumed to be a single power law, $N(a) \propto a^{-3.7}$, as derived by Mathis & Whiffen for interstellar dust grains, but with different truncation values. The smallest grain size is taken to be $a_{min} = 0.03 \mu\text{m}$ (corresponding to a size parameter of $0.05 \lesssim x \lesssim 0.25$) in all models since even smaller grains do not contribute to scattering at visible or near-infrared wavelengths. With respect to the value quoted by Mathis & Whiffen ($a_{min} = 0.005 \mu\text{m}$), this only has an impact on the average dust opacity but the latter is not modified by more than 15%. Since we are interested in constraining the dust grain size distribution, its upper cutoff, a_{max} , was the only parameter that we let vary in our models⁵. We used values of a_{max} ranging from $0.25 \mu\text{m}$ to $3.0 \mu\text{m}$. For each value of a_{max} , the average mass of the grains over the entire size distribution is calculated and the total number of grains is then set so that the total dust mass in the ring remains the same in all simulations.

A complete list of the Monte Carlo simulations we ran is presented in Table 3. Five models (3, 8, 12, 15 and 17) were calculated at all four wavelengths while 4 to 6 additional models were run at each wavelength to ensure a fine sampling around the best fit a_{max} . Overall, 42 different simulations were run. Each synthetic image has been convolved with an appropriate Gaussian kernel so that it has a similar resolution as the observed one.

4.2. Results and general trends from the simulations

The intensity maps for all models that were calculated at all wavelengths are presented in Figure 4. We can readily see that no single model can reproduce simultaneously all the images of the ring, since longer wavelength images seem to require larger values of a_{max} than the I and J images. Before comparing in more detail the models to the observations, we first describe here some generic trends that are nicely illustrated in Figure 4.

The natural dependency of scattering on the ratio of dust grain size to wavelength is clearly illustrated by our numerical simulations. Two models with almost equal a_{max}/λ ratio (for instance model 3 at J band and model 8 at H band) have very similar synthetic images. Generally speaking, the shorter the wavelength and/or the larger a_{max} , the more forward-throwing the scattering. Since the ring is not seen exactly pole-on but tilted by about 37° , forward-throwing scattering results in more flux on the front (Northern) edge of the ring, as is observed in most of our models. The asymmetry parameter, g , is the quantity that

⁵The slope of the grain size distribution is another important parameter describing the dust population. Varying this slope could result in slightly different values for the best fitting a_{max} , but the overall behavior describe below would remain the same.

measures the preference for forward-throwing scattering in Mie theory. Isotropic scattering has $g = 0$ while purely forward-throwing dust grains are characterized by $g = 1$. For each of our models, we define a median asymmetry parameter, $\overline{g_\lambda}$ in the following way: from the scattering probability distribution, we determine what the “median scatterer” size (a_{med}) is, defined so that exactly 50% of all scattering events occur on larger grains. The asymmetry parameter corresponding to this grain size is taken to be $\overline{g_\lambda}$; the value of this parameter for all models are listed in Table 4. As an illustration of isotropic scattering, one can see in Figure 4 that the L' images of models that only contains small grains ($a_{max} \lesssim 0.5 \mu\text{m}$; those models have $\overline{g_{L'}} < 0.1$) have their peak surface brightness on the back (southern) side of the ring, which presents a larger solid angle than the front edge of the ring, as opposed to most other models and to all actual images of the ring.

Our numerical simulations predict significantly redder colors for the ring than for the illuminating stars for almost all models, up to ~ 0.5 mag color excess despite neutral or slightly blue albedo values. We already pointed out this effect in McCabe et al. (2002) and suggested that this was a consequence of the high and strongly wavelength-dependent values of $\overline{g_\lambda}$ for the Mathis & Whiffen (1989) dust model. Here, we find that the models with the larger a_{max} systematically have larger color indices, in agreement with this explanation since they have larger asymmetry parameters.

For each wavelength, we can determine which model best matches the observations. We are particularly interested in analyzing the scattering phase function of the dust grains in the ring, as the latter is strongly dependent on the size of the largest grains in the ring. There are several possible quantitative approaches to comparing the synthetic maps produced by our Monte Carlo simulations and the observed images of the ring. Both the disk/star flux ratio (R_λ) and integrated front/back ratio (FB_λ) are very well defined in the simulations. Therefore, we computed both of these flux ratios for all of the simulations using the same elliptical aperture as defined in § 3. The results are tabulated in Table 4; relative uncertainties are less than 2% as measured from the standard deviation of measurements for two models that were run three times.

While both R_λ and FB_λ depend on the dust scattering phase function, they also are strongly sensitive to the assumed disk geometry. In particular, they depend on the solid angle of the ring as seen from the central star and, because the ring is both optically and geometrically thick, the effect is not the same on the front and back side of the ring. Since we would like to focus on the scattering properties of dust grains, it is not advisable to use quantities that can be strongly affected by uncertain assumptions on the disk geometry. Integrated fluxes are therefore not the best quantities to use in comparing the models to the observations. The peak azimuthal brightness variations offers a better handle on the grains

properties, as it basically traces the single-scattering intensity off an optically thick wall, i.e., essentially the dust scattering phase function. It is much less sensitive to geometric assumptions than integrated flux ratios as scattering angles ranging from $\sim 50^\circ$ (on the norther side of the ring) to $\sim 120^\circ$ (on its southern part) are probed. Fitting the entire azimuthal surface density profile is therefore more appropriate than integrated fluxes or than peak-to-peak flux ratios, which can be corrupted by local perturbations in the structure of the ring.

We therefore adopted the following method, which is based on the azimuthal intensity variations and is illustrated in Figure 2, to determine a range of acceptable models. For each wavelength, we first plotted the observed intensity variations, normalized to the average flux in the position angle range (centered on the disk’s semi-minor axis) $345^\circ\text{--}25^\circ$. Then all models calculated at that wavelength were overplotted and normalized in the same way. A modified χ^2 value was calculated for all models, based on the uncertainties in the observed images⁶ and the typical uncertainty of the numerical simulations, estimated from the standard deviation of the profiles of three independent simulations of the same model. The model that results in the smallest χ^2 is the best match to the observations. We consider models with χ^2 values that are not more than 30% larger than the best models to be acceptable models. In the absence of a proper characterization of the uncertainties’ statistical properties (for both the models and the observations), we did not adopt this threshold based on a robust statistical analysis but we consider that it defines a reasonably conservative range of acceptable models, probably equivalent to a $\sim 3\sigma$ confidence level, as illustrated in Figure 2. Models out of that range usually result in very poor fit of the azimuthal intensity variations.

In order of increasing wavelength, the *I* band image of the ring is best reproduced by models 2, 3 and 5 ($0.275\ \mu\text{m} \leq a_{max} \leq 0.35\ \mu\text{m}$), the *J* band image by models 4–7 ($0.325\ \mu\text{m} \leq a_{max} \leq 0.45\ \mu\text{m}$), the *H* band image by models 7–10 ($0.45\ \mu\text{m} \leq a_{max} \leq 0.6\ \mu\text{m}$) and the *L'* band image by models 14–19 ($1.125\ \mu\text{m} \leq a_{max} \leq 2.5\ \mu\text{m}$). As illustrated in Figure 4, increasingly large dust grains are required to reproduce the images at longer wavelengths. The best fit models systematically underestimate FB_λ and overestimate R_λ . Using either of these two flux ratios would therefore yield a different set of best-fitting dust model. However, the general behavior of increasing a_{max} values being required to reproduce longer wavelength images would still hold. As explained above, we believe that our method is the best to constrain the scattering phase function of dust grains, hence their size, because it is less dependent on the assumed geometry of the ring.

⁶Uncertainties were first calculated for each 10° sector as the standard deviation of the measurements from 3 or 4 sub-images, then averaged over all sectors in a given image of the ring and uniformly assigned to all measurements.

For the models calculated at all wavelengths, we find that the distance between the front edge of the ring and the center of mass of the binary systematically increases with wavelength, as a consequence of the decreasing opacity. For all models, the ratio of opacities is on order of $\kappa_{L'}/\kappa_I \approx 10$, so that scattering at $3.8\ \mu\text{m}$ probes much deeper into the ring. A given τ_λ surface is therefore closer to the disk midplane at longer wavelength and, given the inclination of the ring, it appears closer to the projected inner radius of the ring, i.e. further away from the center of mass of the system. This predicted behavior is also present in the data (see § 3.2) and the simulations predict an amplitude for this effect of $0''.05\text{--}0''.08$, in rough agreement with our geometrical model of the ring.

5. Discussion

In light of our multi-wavelength analysis of the GG Tau ring, both the geometry of the ring and the properties of the dust population in the ring can be studied in much more detail than in previous work. We first show that the slightly revised disk geometry adopted here better matches the observed images (§ 5.1) and then argue that grains larger than those of the interstellar medium are present in the ring, in a stratified configuration (§ 5.2).

5.1. Revisiting the geometry of the system

Most scattered light models of the GG Tau ring are based on the geometry derived from the optically thin millimeter thermal emission by Guilloteau et al. (1999), namely an axisymmetric, low-flaring disk with very sharp inner and outer radii. Here we review some evidence that this geometry might require minor revisions to reproduce the images of the ring.

First, all scattered light images of the system have shown that the ring is not completely smooth and that there are some departures from simple symmetries, such as the “gap” clearly shown by Krist et al. (2002) on the western side of the ring or the displacement between the ring’s brightest point and its semi-minor axis. These could be the result of local density perturbations, such as a gravitational wave at the inner edge of the disk, or of shadowing effects induced by obscuring material located around the stars themselves. Although these perturbations are strong enough to create clear asymmetries in the scattered light images, the absence of azimuthal variations in the optically thin thermal emission of the ring suggests that departures from axisymmetry must be of relatively small amplitude. In our model, we have kept the axisymmetry assumption because it allows a dramatic decrease in the

number of photons needed to run our Monte Carlo simulations thereby enabling a better sampling of the parameter space. Because we use the complete azimuthal intensity variations (using averages within 10° sectors) to compare models to the observed images of the ring, we consider that small scale intensity variations are unlikely to strongly affect our conclusions regarding dust properties.

In our previous modeling effort of the GG Tau ring, we had used essentially the same numerical code and disk geometry, except that we had enforced a strict vertical cutoff to the ring at about 35 AU above the disk midplane (McCabe et al. 2002); no dust grains were present above such an elevation. This was required to match the observed distance between the center of mass of the system and the Northern edge of the ring. Here, we have not used such a cutoff, so that a decreasing amount of material is located even further high above the midplane. There are two direct consequences to the absence of vertical cutoff: i) the synthetic scattered light images have the front edge of the ring too close from the stars by about $0''.10$, and ii) the integrated disk/star flux ratio is too large by a factor of 2–3 with respect to the observations, as opposed to the results of the models with a cutoff. A vertical cutoff therefore appears to be necessary to match the location of the front edge of the ring and the total disk/star flux ratio. However, numerical simulations that include it fail to reproduce the extent of the back side: in all simulations with a cutoff, the back side of the ring does not extend beyond $\sim 1''.2$ of the center of mass along the semi-minor axis (see Figure 5). Since both the visible and near-infrared images clearly show that the back side actually extends $\sim 1''.7$ away from the center of mass, we reject the hypothesis that such a vertical cutoff is actually present in the GG Tau ring.

In the “no-cutoff” model we argue for here, we believe that the disagreement between the predicted and observed values of R_λ can be explained by improper albedo values, which depend more on the dust composition than the scattering phase function, and/or by an unrealistic treatment of self-absorption toward the front edge of the ring, where most of the ring flux comes from. For instance, the vertical distribution of dust may not be gaussian, especially at the ring’s inner edge where a pile-up of material can be expected due to the detailed physics of the gravitational resonance induced by the orbital motion of the binary. For the time being, we believe that this issue does not represent a major shortcoming of our model of the ring. However, the observed distance between the system’s center of mass and the ring front edge is significantly larger than the “no-cutoff” model predicts as pointed out above. To reconcile the models with the observations on this aspect, we have increased the ring’s inner radius from 180 AU to 190 AU and shrank the $1/e$ width inner density drop-off from 7 AU to 2 AU. As illustrated in Figure 5, this results in an excellent match between the observed and predicted images of the ring. This revision to the ring’s inner radius is only marginal and is within 2σ of the best-fitting values derived by Guilloteau et al. (1999).

Furthermore, our numerical simulations show that the increased ring’s inner radius only results in a $\sim 7\%$ loss in the predicted scattered light flux from the ring, i.e., a negligible effect for our analysis. We therefore adopt this new set of parameters in our present analysis.

Another important aspect regarding the geometry of the system is the possible presence of some obscuring material between the binary system and the ring. The observed neutral/red excess color indices of the ring with respect to the stars has led Roddier et al. (1996), Wood et al. (1999) and Krist et al. (2002) to argue that such material is present in order to compensate the intrinsically blue color of scattering. However, as discussed in §4.2, scattering off the optically thick ring can result in red colors depending on the assumed dust properties. Using our best fit models for each image of the ring, which have been determined independently of the ring’s flux and color indices, we predict color excesses with respect to the central sources of $\Delta(I - J) = 0.06$ mag, $\Delta(J - H) = -0.01$ mag and $\Delta(H - L') = -0.11$ mag, in reasonable agreement with the observed values to within 0.1–0.2 mag. This suggests that there is only little extinction between the stars and the ring. The large $\Delta(V - I) = 0.8$ mag color excess found by Krist et al. (2002) supports a moderate extinction in the plane of the ring. Their V -band image of the ring lacks the signal-to-noise to allow model fitting unfortunately, so we cannot determine the best-fitting model at that wavelength. Still, *if* the region of the ring probed by scattered light at V is identical to that probed at I (or if those two regions contain the same dust population), we predict a color excess of $\Delta(V - I) = 0.28$ mag (see Table 4), which is not as red as the observations of the ring. The remaining color excess, $\Delta(V - I) \sim 0.5$ mag, corresponds to an in-the-plane extinction of $A_V \approx 1.0$ mag assuming an $R_V = 3.1$ extinction law (Rieke & Lebofski 1985). Overall, the observed colors of the GG Tau ring are consistent with a system’s geometry in which there is a moderate amount of reddening between the stars and the ring. Note that the absence in all images of the “dark central lane” on the back side of the ring, as predicted by Wood et al. (1999) assuming coplanar optically thick circumstellar disks, also requires that extinction in the plane of the ring must be optically thin.

5.2. A stratified dust population

As pointed out in §3.2, the azimuthal distribution of scattered light is remarkably similar in all images of the ring over a factor of 4 in wavelength, from I to L' . This suggests that the scattering properties of the dust grains, in particular their phase function, evolves only marginally over this wavelength range. This is in sharp contrast with all models of ISM grains, which have $a_{max} \leq 1 \mu\text{m}$ and, therefore, are much more forward throwing in the visible than in the near-infrared (Kim et al. 1994; Zubko, Krelowski & Wegner 1998). In the

following, we use the range of acceptable phase function asymmetry parameters we found at each wavelength (§ 4.2) to constrain the dust grain size distribution in the ring and we argue that it is likely that the ring has a stratified structure, in which larger grains are present closer to the disk midplane.

First of all, an important qualitative statement can be readily made in the framework of our assumed dust model: since we find no value of a_{max} that matches all images of the ring simultaneously, we conclude that the size distribution in the ring is not a simple power law, and/or that the dust population in the ring is not uniform. The latter explanation would be the correct one if each wavelength was probing a different region of the disk with its specific size distribution. While we found that the L' image of the ring probes deeper into the disk than shorter wavelength images, we have also shown that all images at $0.8 \mu\text{m} \leq \lambda \leq 1.6 \mu\text{m}$ probe the same region of the ring, located about 50 AU above its midplane. However, the acceptable models for reproducing the H band image disagree significantly with the I and J images of the ring. Therefore, we can exclude that the surface layer of the ring contains a single power law size distribution.

Before exploring the possibility of spatially-dependent grain properties, we first attempt to find a refined dust model that reproduces all the images of the ring under the assumption of an homogeneous dust population throughout the ring. In particular, we would like to find a dust model that matches the entire \overline{g}_λ curve derived for the GG Tau ring. While our models of the ring, which assume azimuthal symmetry and power law grain size distributions, may be too simplistic, we believe that we are properly probing the scattering phase function of the dust grains, so that our derived values of \overline{g}_λ are probably close matches to that of the actual grain population⁷. Figure 6 summarizes our results regarding the dust grains in the GG Tau ring, as well as some frequently used ISM dust models (Mathis & Whiffen 1989; Weingartner & Draine 2001). It is important to realize that, for these ISM dust models, the scattering phase function is calculated after a model is fit to the general ISM *extinction/emission* law defined by $R_V = 3.1$, whereas our analysis of the GG Tau ring dust population provides *direct* estimates of \overline{g}_λ . In this context, it is noteworthy that two different models reproducing the same ISM extinction law can have asymmetry parameters that differ so much. This results from the different assumptions made on the dust composition and shape of the size

⁷Krist et al. (2002) derived $\overline{g}_I = 0.65$ from their image of the ring, which is just outside of the range we have accepted here. While this is probably not significant, we note that their best fit value is obtained by matching the maximum peak-to-peak flux ratio between the front and back side of the ring, whereas we consider the entire azimuthal intensity variations. These slightly different methods probably explains the small disagreement between the two best fit values of \overline{g}_I . Note that our method is intrinsically less likely to be affected by small scale intensity variations in the ring.

distribution but, as shown in Figure 6, this raises doubts about which model best matches the ISM dust population. Independently of this unsolved ambiguity, the observed shape of the $\overline{g_\lambda}$ curve for the GG Tau ring cannot be matched by any current ISM dust model. Larger dust grains are required to match the value of $\overline{g_{L'}}$ derived in this study, as evidenced by the 1.125–2.5 μm upper limit for the size distribution we have found assuming a simple power law for the size distribution. Even larger grains may be present in the ring provided that the size distribution has a more complex shape, such as the $N(a) \propto a^{-p}e^{-(a/a_c)}$ form sometimes used for ISM models (e.g., Kim et al. 1994; Clayton et al. 2003).

This need for a significant population of grains larger than 1 μm is reminiscent of the dust models developed to reproduce the extinction curves measured through molecular clouds, which are likely to contain the precursor material of future circumstellar/binary disks. As illustrated in Figure 6, the model derived by Weingartner & Draine (2001) to reproduce an $R_V = 5.5$ extinction law provides a good match to the asymmetry parameters at I and J and is only slightly off the range of acceptable models at H . However, this model predicts too low a value for $\overline{g_{L'}}$, even though it contains grains as large as 10 μm . In other words, the grain size distribution inferred for molecular cloud does not contain *enough* grains larger than 1 μm to reproduce our L' image of the GG Tau ring, suggesting that further growth of the dust grains (or a relative depletion of the smaller particles) has occurred in the ring.

The only dust model we are aware of that resembles the observed wavelength dependence of $\overline{g_\lambda}$ is the model that Wood et al. (2002) constructed to reproduce the entire spectral energy distribution of HH 30, a young stellar object that is surrounded by an opaque, edge-on circumstellar disk. This model does not provide a perfect match however, as it systematically overestimates the asymmetry parameters at wavelengths $\lambda \lesssim 1.6 \mu\text{m}$ (Figure 6). Still, this suggests that a model in which the dust population of the ring is spatially uniform and has a size distribution similar to that found by Wood et al. for another equally young object, i.e., extending up to $\sim 1 \text{ mm}$, could reproduce the various images of the GG Tau ring.

An independent empirical test can be performed regarding the dust population of the GG Tau ring based on the *HST*/NICMOS 1 μm polarization map obtained by Silber et al. (2000), which probes the surface layer of the ring. The dust grain size distribution not only dictates the scattering phase function, it also determines the maximum linear polarization rate for a single 90°-scattering event. Recently, Whitney et al. (2003) have calculated the maximum polarization rates corresponding to ISM and molecular cloud dust grains, as well as to a dust model containing somewhat larger grains that has been devised to reproduce the near-infrared scattered light images of HH 30 (Cotera et al. 2001) and, finally, to the dust model proposed by Wood et al. (2002). At 1 μm , they find a maximum polarization rate of 50-55% for both ISM and molecular cloud-like dust models but only $\sim 40\%$ for

the latter two models. The lower polarization rate in the models containing larger dust grains is a consequence of the larger polarizing efficiency of small dust grains in the Rayleigh regime. The polarization map of Silber et al. (2000) peaks at $\sim 50\%$ for a scattering angle of $\sim 100^\circ$. This must be considered as a lower limit to the actual single-scattering maximum rate in particular because of the diluting effect of multiple scattering on the linear polarization. Therefore, only ISM- and molecular cloud-like dust models can account for such high polarization rates as observed in the ring, ruling out the possibility of much larger grains in its surface layer.

To summarize, we find that a dust model similar to those derived for molecular cloud environments can simultaneously reproduce the images of the ring at all wavelengths shorter than $1.6\ \mu\text{m}$ as well as the $1\ \mu\text{m}$ polarization map of the GG Tau ring. However, the new L' image of the ring presented here requires much larger dust grains, supporting a model that is on the other hand unable to reproduce all of the shorter wavelength constraints. More explicitly, it appears that the $\sim 50\%$ linear polarization rate observed at $1\ \mu\text{m}$ is incompatible with the highly forward-throwing scattering observed at $3.8\ \mu\text{m}$. Combined with the fact that the L' scattered light image probes a different layer of the ring than the shorter wavelength datasets (§5.1), this implies that the dust grain properties are not uniform throughout the ring. Namely, the surface layer of the ring, located $\sim 50\ \text{AU}$ above its midplane, contains a dust population that is very similar to that observed in dense molecular clouds whereas the layer of the ring located twice as close to the midplane, which is probed by our new thermal infrared image, contains significantly larger grains. Exactly how large the dust grains are depends on the exact shape of the size distribution and on the dust composition. Indeed, a single power-law distribution with $a_{max} \sim 1.5\ \mu\text{m}$ and a Mathis & Whiffen (1989) composition leads to essentially the same value of $\overline{g_{L'}}$ as the amorphous carbon and silicate model of Wood et al. (2002) that extends up to $1\ \text{mm}$ in radius. Although we cannot yet fully determine the dust grain properties in the deeper layers of the ring, we can tell that they contains dust grains larger than $\sim 1\ \mu\text{m}$ in size in non-negligible amounts, which is not true for the surface of the ring.

Interestingly, the shallow opacity law for the ring ($\kappa_\nu \propto \nu^\beta$, with $\beta = 1.15 \pm 0.10$) found by Guilloteau et al. (1999) is similar to that predicted by the dust model of Wood et al. (2002), another argument favoring this dust model for the bulk of the dust component of the ring. This is indeed one of the first times that a dust model with very large grains ($a_{max} \sim 1\ \text{mm}$), such as frequently supported by thermal millimeter emission, is consistent with a scattered light image. In other well-studied T Tauri disks, like those of HH 30 or TW Hya, only the long wavelength thermal emission requires such large grains to be present, whereas all scattered light images are well represented by dust grains that are not significantly larger than those found in molecular clouds (e.g., Burrows et al. 1996; Cotera et al. 2001;

Weinberger et al. 2001).

The only other disk for which scattered light images have called for much larger dust grains than the ISM is HK Tau B, whose scattered light disk as seen in the visible is well reproduced with ISM-like dust grains (Stapelfeldt et al. 1998) while a recent mid-infrared scattered light has led to the conclusion that it also contains much larger grains (McCabe et al. 2003). While the analysis of the thermal emission from this object is still under debate (D’Alessio et al. 2001; Duchêne et al. 2003), we note that the dust model developed by Wood et al. (2002) is fully consistent with the highly forward-throwing scattering properties observed at $12\ \mu\text{m}$ by McCabe et al. (2003). The fact that only long wavelength ($\lambda > 3\ \mu\text{m}$) scattered light images of protoplanetary disks require the presence of multi-micron dust grains is in part a consequence of the wavelength-dependence of scattering. However, it can also be interpreted as evidence that the surface layers of protoplanetary disks usually contain ISM and/or molecular cloud-like dust populations whereas the deeper regions of these disks, probed by millimeter thermal emission and now also by thermal- and mid-infrared scattering, contain much larger grains. In this picture, we predict that long wavelength scattered light images of other protoplanetary disks such as HH 30 or TW Hya will reveal highly forward-throwing, hence much larger, dust grains.

Stratified disk models have already been studied in the context of protoplanetary disks (e.g., Chiang et al. 2001; Lachaume et al. 2003) and have been proposed for several systems (Weinberger et al. 2002; Duchêne et al. 2003). The physical cause for this stratification of the ring could be i) preferred dust coagulation in the disk midplane, where the density and therefore the grain-grain interaction probability are highest, and/or ii) gravitational settling of the largest, hence most massive, grains which cannot be prevented from falling toward the midplane by turbulence or gas heating. It is not possible for now to distinguish between these two options, except for the fact that we have shown that the surface layers of the GG Tau ring contains almost no grains larger than those found in molecular cloud, i.e., they appear to constitute an unevolved dust population. If larger grains had grown there, it may be difficult to explain why only those grains that have formed in the process have sunk unless turbulence in the disk is strong enough to maintain the small grains in suspension high above the midplane. On the other hand, our best model of the ring implies that the volume density of grains is only 5 times larger at an elevation of 25 AU with respect to the (surface) 50 AU layer. It is unclear whether such a modest change in density is enough to trigger significant grain growth through grain-grain interaction.

From the similarity between the dust properties contained in the ring’s surface layer and those of a typical molecular cloud, one may conclude that only marginal grain growth has occurred in the pre-collapse dense core that led to the formation of the binary system.

In this context, the dust grains probed by the shortest wavelength scattered light images can be considered as pristine, while the larger dust grains required to explain our observed L' image of the ring, as well as its millimeter thermal emission properties, imply that grain growth has occurred deeper in the ring, in its highest density regions, after it was initially formed. While this may not seem surprising, it is noticeable that, as opposed to most young disks in which grain growth has been suggested in the past, we extend this conclusion to a much wider, circumbinary structure, whose dynamical timescale is on order of 2000 yrs instead of a few decades. One could therefore have expected grain growth to be a much slower phenomenon in this ring. For instance, the dust evolution model of Suttner & Yorke (2001), which can lead to very large grains in $\sim 10^4$ yrs within 30 AU of the central star, predicts almost no change of the dust size distribution at a radius of 200 AU over the same timescale. The dynamical timescale is about 20 times longer at this radius, so a similar growth could require a few 10^5 yrs, only a few times younger than the GG Tau system itself. Still, our thermal infrared image of the system suggests that significant grain growth has already occurred in the ring.

6. Conclusion

Using the AO system on the W. M. Keck II 10 m-telescope, we have obtained the first $3.8 \mu\text{m}$ scattered light image of the circumbinary dusty torus around the young binary system GG Tau. This is the longest wavelength at which the ring has been imaged in scattered light so far. The ring surface brightness variations appear to be remarkably similar to those observed in the visible and near-infrared in previous *HST* studies of the system, suggesting that the scattering properties of dust grains in the ring are barely dependent on wavelength, a distinctly different behavior when compared to ISM dust models. We also find that the scattered light from the front edge of the ring, which traces the upper optically thick layers above the ring's midplane, is projected further away from the center of mass of the system at L' than in shorter wavelength images. This is consequence of the reduced dust opacity at $3.8 \mu\text{m}$ and it allows us to probe for the first time the dust scattering properties only 25 AU above the midplane, instead of 50 AU above it in previous studies.

Using a Monte Carlo multiple scattering numerical code, we have conducted a multi-wavelength modeling analysis of the scattered light images of the ring in an attempt to study in more detail both the geometry of the ring and the properties of the dust grains it contains. We find that all images are best reproduced with a slightly increased inner radius (190 AU instead of 180 AU) and steeper density fall-off inside of this radius. Our best fit models, although they systematically predict ~ 3 times too much scattered flux from the ring, result

in excess color indices with respect to the central stars from I to L' that are consistent with the observations within 0.1–0.2 mag typically. The predicted $V - I$ color of the ring falls short of the observed one, however, suggesting that there is a limited amount of reddening ($A_V \approx 1.0$ mag) between the stars and the ring.

By comparing the azimuthal intensity variations of our models to the observations, we have identified a range of possible dust models at each wavelength assuming a simple power law size distribution. While this likely is too simplistic an assumption, it allows us to constrain the phase function asymmetry parameters of the dust population at each wavelength. Our best fit models have asymmetry parameters $\overline{g_\lambda} \approx 0.4$ –0.5 at all wavelength from I to L' . No ISM dust models are compatible with such a behavior, nor are models representing the dust grain population present in dense molecular clouds. The latter are consistent with the I , J and H image of the ring (though a pure power law size distribution is not) but not with the new L' image presented here. The only dust model that is consistent with all images of the ring is that developed by Wood et al. (2002) to reproduce the spectral energy distribution of another protoplanetary disk. However, this model predicts a $1 \mu\text{m}$ linear polarization rate that is much smaller than what has been observed for the GG Tau ring.

We therefore propose that the GG Tau ring contains more or less unprocessed molecular cloud-like dust grains in its surface layers, ~ 50 AU above the midplane, while significantly larger dust grains are present deeper into the disk, in agreement with the millimeter thermal emission from the system. We suggest that this stratified structure is a general feature of protoplanetary disks and could be the result of dust settling and/or preferred grain coagulation in the deeper, densest parts of the disks. We also conclude that large grains have grown in size in this large circumbinary ring despite its much longer dynamical timescale with respect to typical circumstellar disks where this has already been suggested in the past.

We are grateful to the W. M. Keck Observatory personnel whose professional and efficient help during our run allowed us to obtain such high quality data as presented in this paper. In particular, we thank Randy Campbell, Gary Puniwai, David le Mignant, Peter Wizinowich and Tim Saloga. We also want to thank John Krist for making his calibrated *HST*/WFPC2 I band images of GG Tau available to us for analysis. This work has been supported by the National Science Foundation Science and Technology Center for Adaptive Optics, managed by the University of California at Santa Cruz under cooperative agreement No. AST - 9876783, and by the Packard Foundation. Data presented herein were obtained at the W.M. Keck Observatory, which is operated as a scientific partnership among the California Institute of Technology, the University of California and the National Aeronautics and Space Administration. The Observatory was made possible by the generous financial

support of the W.M. Keck Foundation. The authors wish to recognize and acknowledge the very significant cultural role and reverence that the summit of Mauna Kea has always had within the indigenous Hawaiian community. We are most fortunate to have the opportunity to conduct observations from this mountain.

REFERENCES

- Beckwith, S. V. W., Sargent, A. I., Chini, R. S. & Guesten, R. 1990, *AJ*, 99, 924
- Beckwith, S. V. W. & Sargent, A. I. 1991, *ApJ*, 381, 250
- Bertout, C., Robichon, N. & Arenou F. 1999, *A&A*, 352, 574
- Bouchet, P., Schmider, F. X. & Manfroid, J. 1991, *A&AS*, 91, 409
- Burrows, C. J., Stapelfeldt, K. R., Watson, A. M., Krist, J. E., Ballester, G. E., Clarke, J. T., Crisp, D., Gallagher, J. S. III, Griffiths, R. E., Hester, J. J., Hoessel, J. G., Holtzman, J. A., Mould, J. R., Scowen, P. A., Trauger, J. T. & Westphal, J. A. 1996, *ApJ*, 473, 437
- Chiang, E. I., Joung, M. K., Creech-Eakman, M. J., Qi, C., Kessler, J. E., Blake, G. A. & van Dischoeck, E. F. 2001, *ApJ*, 547, 1077
- Clayton, G. C., Wolff, M. J., Sofia, U. J., Gordon, K. D. & Misselt, K. A. 2003, *ApJ*, 588, 871
- Cotera, A. S., Whitney, B. A., Young, E., Wolff, M. J., Wood, K., Povich, M., Schneider, G., Rieke, M. & Thompson, R. 2001, *ApJ*, 556, 958
- D'Alessio, P., Calvet, N. & Hartmann, L. 2001, *ApJ*, 553, 321
- Duchêne, G. 2000, Ph.D. thesis, Univ. Grenoble
- Duchêne, G., Ménard, F., Stapelfeldt, K. R. & Duvert, G. 2003, *A&A*, 400, 559
- Ghez, A. M., Neugebauer, G. & Matthews, K. 1993, *AJ*, 106, 2005
- Guilloteau, S., Dutrey, A. & Simon, M. 1999, *A&A*, 348, 570
- Haisch, K. E. Jr., Lada, E. A. & Lada, C. J. 2001, *ApJ*, 553, L153
- Hartigan, P. & Kenyon, S. J. 2003, *ApJ*, 583, 334

- Itoh, Y., Tamura, M., Hayashi, S. S., Oasa, Y., Fukagawa, M., Kaifu, N., Suto, H., Murakawa, K., Doi, Y., Ebizuka, N., Naoi, T., Takami, H., Takato, N., Gaessler, W., Kanzawa, T., Hayano, H., Kamata, Y. & Saint-Jacques, D. 2002, PASJ, 54, 963
- Kenyon, S. J. & Hartmann, L. 1995, ApJS, 101, 117
- Kenyon, S. J. & Bromley, B. C. 2003, AJ, in press
- Kim, S.-H., Martin, P. G. & Hendry, P. D. 1994, ApJ, 422, 164
- Krist, J. E., Stapelfeldt, K. R. & Watson, A. M. 2002, ApJ, 570, 785
- Lachaume, R., Malbet, F. & Monin J.-L. 2003, A&A, 400, 185
- Leinert, C., Haas, M., Mundt, R., Richichi, A. & Zinnecker, H. 1991, A&A, 250, 407
- McCabe, C., Duchêne, G. & Ghez, A. M. 2002, ApJ, 575, 974
- McCabe, C., Duchêne, G. & Ghez, A. M. 2003, ApJ, 588, L113
- Mannings, V. & Emerson, J. P. 1994, MNRAS, 267, 361
- Mathis, J. S. & Whiffen, G. 1989, ApJ, 341, 808
- Ménard, F. 1989, PhD. thesis, Univ. Montréal
- Pollack, J. B., Hubickyj, O., Bodenheimer, P., Lissauer, J. J., Podolak, M. & Greenzweig, Y. 1996, Icar., 124, 62
- Press, W. H., Teukolsky, S. A., Vetterling, W. T. & Flannery, B. P. 1992, *Numerical recipes in C* (2nd ed.), Cambridge Univ. Press
- Roddier, C. Roddier, F., Northcott, M. J., Graves, J. E. & Jim, K. 1996, ApJ, 463, 326
- Safranov, V. S. 1969, “Evolution of the Protoplanetary Cloud and Formation of the Earth and Planets” (Moscow: Nauka) (English transl. 1972, NASA TT F-677)
- Silber, J., Gledhill, T., Duchêne, G. & Ménard, F. 2000, ApJ, 536, L89
- Simon, M. & Guilloteau, S. 1992, ApJ, 397, L47
- Stapelfeldt, K. R., Krist, J. E., Ménard, F., Bouvier, J., Padgett, D. L. & Burrows, C. J. 1998, ApJ, 502, L65
- Suttner, G. & Yorke, H. W. 2001, ApJ, 551, 461

- Tinney, C. G., Mould, J. R. & Reid, I. N. 1993, *AJ*, 105, 1045
- Weidenschilling, S. J. 1980, *Icar.*, 44, 172
- Weinberger, A. J., Becklin, E. E., Schneider, G., Chiang, E. I., Lowrance, P. J., Silverstone, M., Zuckerman, B., Hines, D. C. & Smith, B. A. 2002, *ApJ*, 566, 409
- Weingartner, J. C. & Draine, B. T. 2001, *ApJ*, 548, 296
- Weis, E. W. 1996, *AJ*, 112, 2300
- Wetherill, J. W. & Stewart, G. R. 1993, *Icar.*, 106, 190
- White, R. J., Ghez, A. M., Reid, I. N. & Schultz, G. 1999, *ApJ*, 520, 811
- White, R. J. & Ghez, A. M. 2001, *ApJ*, 556, 265
- Whitney, B. A., Wood, K., Bjorkman, J. E. & Wolff, M. J. 2003, *ApJ*, 591, 1049
- Wizinowich, P., Acton, D. S., Shelton, C., Stomski, P., Dathright, J., Ho, K., Lupton, W., Tsubota, K., Lai, O., Max, C., Brase, J., An, J., Avicola, K., Olivier, S., Gavel, D., Macintosh, B., Ghez, A. & Larkin, J. 2000, *SPIE*, 112, 315
- Wood, K., Crosas, M. & Ghez, A. 1999, *ApJ*, 516, 335
- Wood, K., Wolff, M. J., Bjorkman, J. E. & Whitney, B. 2002, *ApJ*, 564, 887
- Zubko, V. G., Krelowski, J. & Wegner, W. 1998, *MNRAS*, 294, 548

Table 1. Properties of the GG Tau binary system.

Sep.	$0''.2507 \pm 0''.0015$
P.A.	$346^\circ 0 \pm 1^\circ 5$
L'_A	6.72 ± 0.13
L'_B	7.31 ± 0.13
$\Delta L'$	0.59 ± 0.03

Note. — The uncertainty in both components L' magnitude include the uncertainty in the absolute photometric calibration whereas the uncertainty on the flux ratio does not.

Table 2. Observed properties of the GG Tau ring.

Filter	I	J	H	L'
λ (μm)	0.81	1.00	1.55	3.78
R_λ (%)	1.30 ± 0.03	1.40 ± 0.03	1.54 ± 0.03	0.97 ± 0.09
FB_λ	1.80 ± 0.03	1.41 ± 0.03	1.39 ± 0.02	~ 2.5
D_{peak} ($''$)	0.87 ± 0.01	0.88 ± 0.1	0.90 ± 0.01	0.97 ± 0.01
g_{fit}	$0.52^{+0.12}_{-0.07}$	$0.47^{+0.19}_{-0.05}$	$0.41^{+0.14}_{-0.07}$	$0.50^{+0.27}_{-0.14}$

Note. — R_λ is the total disk/star flux ratio whereas FB_λ is the integrated front/back ratio for the disk. D_{peak} is the smallest distance (typically measured around position angle 5–15°) between the center of mass of the system and the peak intensity in radial profiles of the ring. All of these quantities for the J and H images are from McCabe et al. (2002) and those for I band are from our reanalysis of the image obtained by Krist et al. (2002). Finally, g_{fit} represents the asymmetry parameter of the best-fitting dust model as defined in § 4.2; the associated “uncertainties” indicates the tolerable range of models.

Table 3. List of all Monte Carlo simulations.

Model	a_{max} (μm)	Filter	Model	a_{max} (μm)	Filter
1	0.25	I	11	0.7	H
2	0.275	I	12	0.9	IJHL'
3	0.3	VIJHL'	13	1.05	L'
4	0.325	J	14	1.125	L'
5	0.35	IJ	15	1.25	IJHL'
6	0.4	IJH	16	1.375	L'
7	0.45	IJH	17	1.5	IJHL'
8	0.5	IJHL'	18	2.0	L'
9	0.55	IH	19	2.5	L'
10	0.6	H	20	3.0	L'

Table 4. Quantities extracted from the Monte Carlo simulations.

λ	Model	a_{med} (μm)	$\overline{g_\lambda}$	R_λ	FB_λ	χ^2	λ	Model	a_{med} (μm)	$\overline{g_\lambda}$	R_λ	FB_λ	χ^2
<i>V</i>	3	0.205	0.73	0.0263	1.68	...	<i>H</i>	3	0.235	0.16	0.0501	0.36	73.8
<i>I</i>	1	0.184	0.38	0.0377	0.72	16.9		6	0.304	0.27	0.0402	0.58	26.7
	2	<i>0.200</i>	<i>0.45</i>	<i>0.0363</i>	<i>0.83</i>	<i>11.7</i>		7	<i>0.336</i>	<i>0.34</i>	<i>0.0377</i>	<i>0.72</i>	<i>18.2</i>
	3	0.216	0.52	0.0339	0.93	11.3		8	0.367	0.41	0.0357	0.87	14.6
	5	<i>0.247</i>	<i>0.64</i>	<i>0.0306</i>	<i>1.14</i>	<i>12.9</i>		9	<i>0.399</i>	<i>0.48</i>	<i>0.0339</i>	<i>1.02</i>	<i>18.9</i>
	6	0.278	0.71	0.0277	1.35	15.3		10	<i>0.431</i>	<i>0.55</i>	<i>0.0323</i>	<i>1.14</i>	<i>18.7</i>
	7	0.307	0.73	0.0255	1.52	14.9		11	0.495	0.67	0.0286	1.37	22.3
	8	0.335	0.75	0.0235	1.70	17.7		12	0.614	0.74	0.0232	1.75	30.8
	9	0.362	0.78	0.0217	1.83	18.8		15	0.803	0.83	0.0180	2.16	33.6
	12	0.529	0.87	0.0142	2.24	20.0		17	0.927	0.86	0.0153	2.26	32.3
	15	0.655	0.91	0.0114	2.33	20.8	<i>L'</i>	3	0.242	0.003	0.0745	0.25	44.2
	17	0.719	0.92	0.0099	2.26	24.1		8	0.400	0.008	0.0612	0.30	31.5
<i>J</i>	3	0.222	0.36	0.0387	0.74	17.2		12	0.692	0.24	0.0407	0.59	13.2
	4	<i>0.238</i>	<i>0.42</i>	<i>0.0365</i>	<i>0.82</i>	<i>13.6</i>		13	0.789	0.31	0.0372	0.77	8.52
	5	0.254	0.47	0.0359	0.99	13.0		14	<i>0.837</i>	<i>0.36</i>	<i>0.0363</i>	<i>0.87</i>	<i>6.63</i>
	6	<i>0.285</i>	<i>0.58</i>	<i>0.0322</i>	<i>1.08</i>	<i>13.6</i>		15	<i>0.915</i>	<i>0.43</i>	<i>0.0344</i>	<i>1.04</i>	<i>6.70</i>
	7	<i>0.317</i>	<i>0.66</i>	<i>0.0297</i>	<i>1.29</i>	<i>15.1</i>		16	0.995	0.50	0.0324	1.17	5.75
	8	0.348	0.71	0.0272	1.43	17.6		17	<i>1.076</i>	<i>0.58</i>	<i>0.0306</i>	<i>1.35</i>	<i>5.86</i>
	12	0.561	0.85	0.0170	2.10	23.3		18	<i>1.387</i>	<i>0.72</i>	<i>0.0246</i>	<i>1.74</i>	<i>6.41</i>
	15	0.712	0.89	0.0129	2.33	23.7		19	<i>1.670</i>	<i>0.77</i>	<i>0.0205</i>	<i>2.04</i>	<i>7.18</i>
	17	0.799	0.91	0.0113	2.50	24.2		20	1.937	0.82	0.0178	2.41	7.92

Note. — $\overline{g_\lambda}$ is the asymmetry parameter of the phase function for the median scatterer, whose size is a_{med} ; this is an input to the numerical simulations and not one of their results. χ^2 measures the quality of the fit to the azimuthal intensity profile of the ring; the boldfaced entries indicate the best-fit models while the italicized ones represent acceptable models (see text for details).

Fig. 1.— *Left*: Final shift-and-add image of the GG Tau system, displayed on a logarithmic scale. North is up and East to the left. *Right*: PSF-subtracted image of the ring, displayed on a square root stretch from the ring’s brightest point down to zero, after smoothing by median averaging pixels in a sliding 3 pixel-radius aperture.

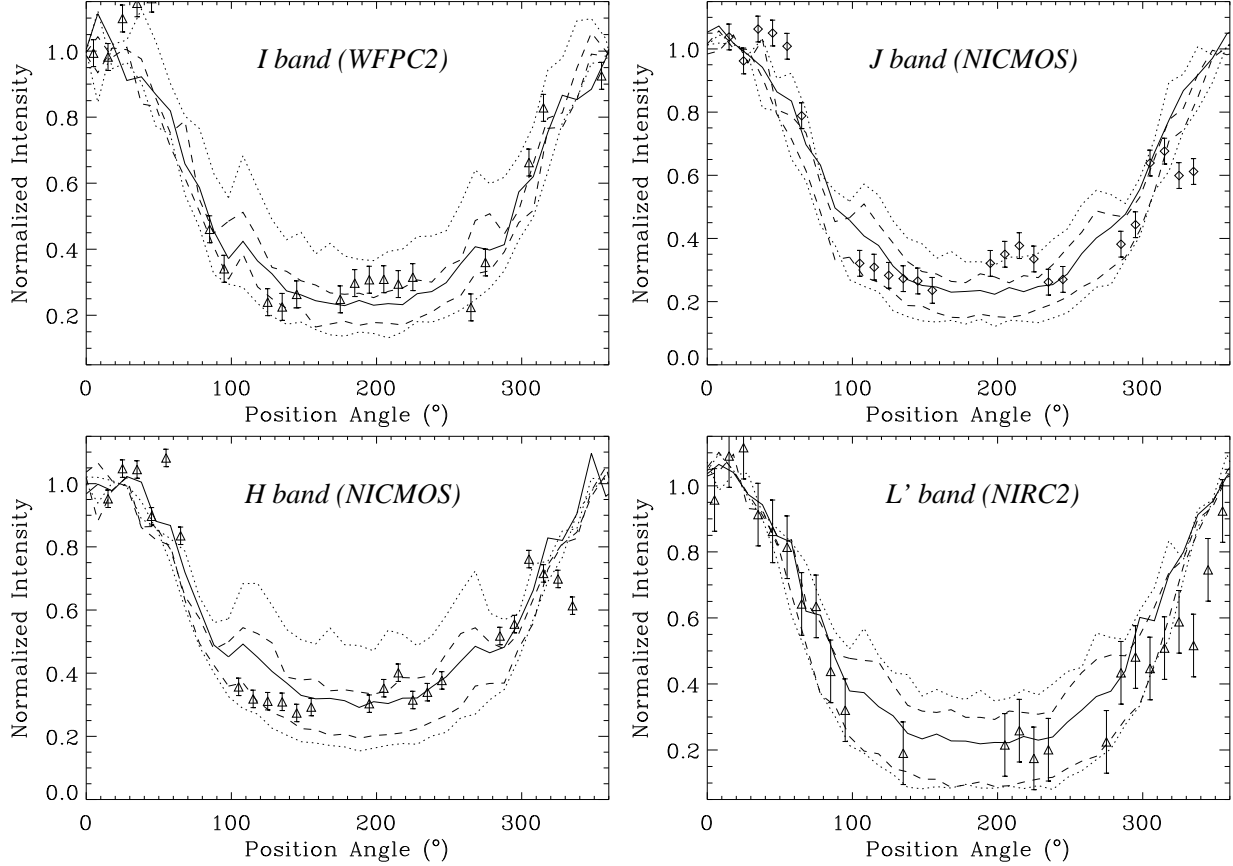


Fig. 2.— Azimuthal intensity profiles of the GG Tau circumbinary disk. Each profile has been normalized to the average flux in the position angle range 345° – 25° , which is centered on the disk semi-minor axis. The solid curves indicates our best matching Monte Carlo simulation while dashed and dotted lines indicate the range of acceptable and the closest unacceptable models, respectively (see § 4.2).

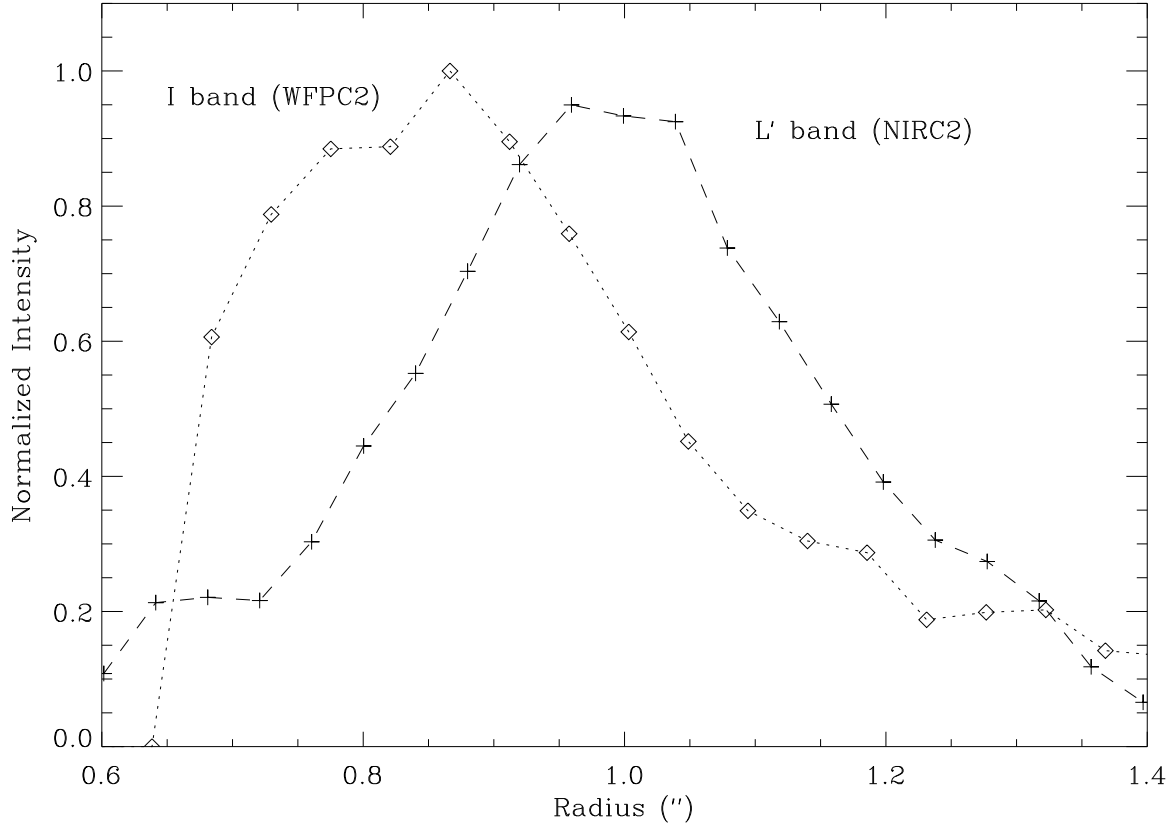


Fig. 3.— Observed radial intensity profiles in a 10° -sector centered on the ring’s northern semi-minor axis (around position angle 5°). Radii are measured from the center of mass of the system in both cases; the central $0''.6$ of both profiles have been masked out as they are dominated by PSF subtraction residuals. The diamonds and dashed line represent the profile observed in the WFPC2 *I* band image whereas the crosses and dashed line show the profile from our *L'* image of the ring. Both profiles are sampled with the corresponding instrument’s pixel scale ($0''.0456$ for WFPC2 and $0''.009942$ for NIRC2).

Fig. 4.— *Left:* PSF subtracted images of the GG Tau ring at I (Krist et al. 2002), J and H (McCabe et al. 2002) and L' (this work), from top to bottom. *Right:* Synthetic intensity maps from the five Monte Carlo models that were calculated at all wavelengths. The respective values of a_{max} are indicated in parentheses. All images have been rotated so that North is up and East to the left and are $4''.2 \times 3''.4$ in size. The grayscale is linear from zero to the peak of the ring in all cases.

Fig. 5.— H band images of the GG Tau system emphasizing the need for a revised geometry of the ring: **a**: Observed image (McCabe et al. 2002); **b**: synthetic map for model 9 with $R_{in} = 180$ AU and a $1/e$ width of 7 AU inside of this radius; **c**: same model with an artificial cutoff of the ring 35 AU above its midplane; **d**: same model without cutoff but with $R_{in} = 190$ AU and a interior $1/e$ width of only 2 AU. The dashed lines, traced for guiding the eye, represent the location of the peak of the ring along its semi-minor axis (upper line) and the point furthest away from the center of mass of the system (lower line). All images are plotted on the same linear gray scale and $4''.2 \times 3''.4$ size.

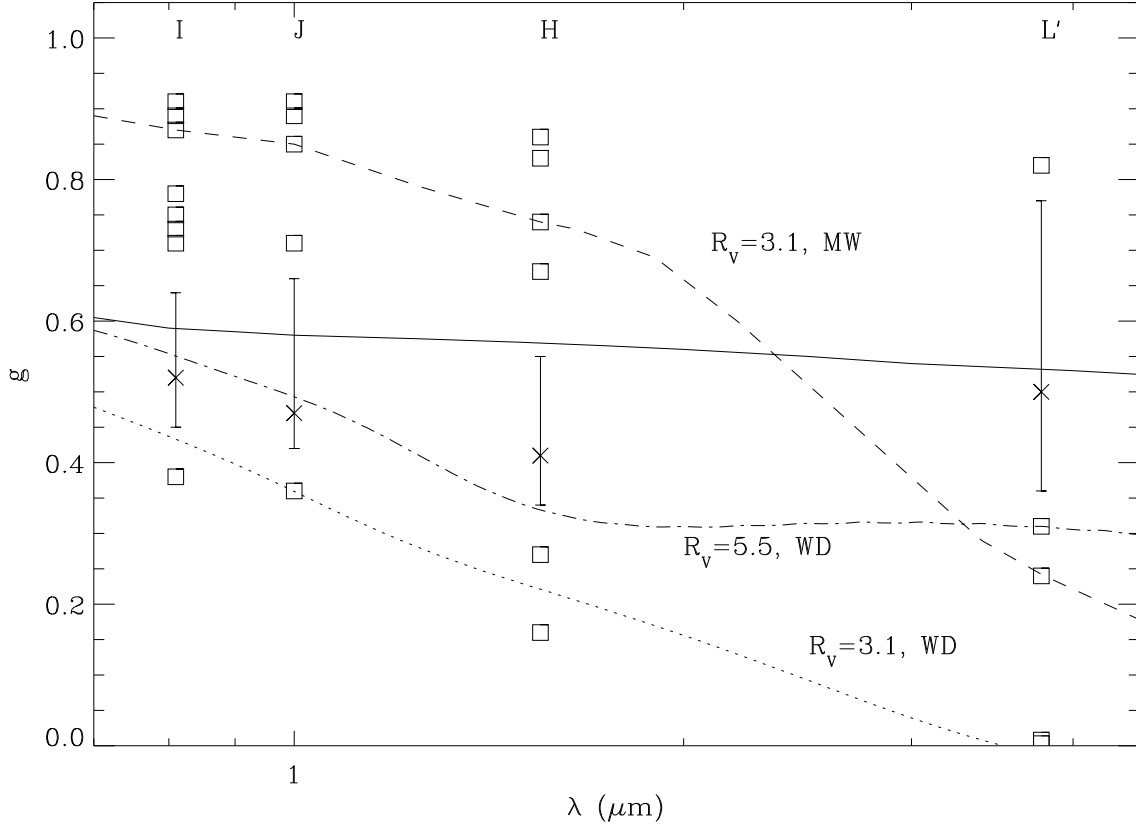


Fig. 6.— Fitted values of the phase function asymmetry parameter for the dust grain population in the GG Tau ring. Crosses indicate the best matching models and the acceptable ranges are indicated as solid segment; these represent $\sim 3\sigma$ confidence intervals. Open squares are models that can confidently be excluded. The dashed line is the predicted dependence of g for the dust grain models developed by Mathis & Whiffen (1989) to match the interstellar ($R_V = 3.1$) extinction law. The dotted and dot-dashed curves are the predicted behaviors of the dust models developed by Weingartner & Draine (2001) for $R_V = 3.1$ and $R_V = 5.5$ extinction laws, respectively. The solid curve is the dust model derived by Wood et al. (2002) to match the spectral energy distribution of the edge-on circumstellar disk system HH 30. Note that the various wavelengths analyzed here for GG Tau do not necessarily probe a single dust population.

This figure "f1.jpg" is available in "jpg" format from:

<http://arxiv.org/ps/astro-ph/0401560v1>

This figure "f4.jpg" is available in "jpg" format from:

<http://arxiv.org/ps/astro-ph/0401560v1>

This figure "f5.jpg" is available in "jpg" format from:

<http://arxiv.org/ps/astro-ph/0401560v1>